

## Bidirectional Elastic Diode with Frequency-Preserved Nonreciprocity

Xin Fang<sup>1,2</sup>, Jihong Wen,<sup>1,\*</sup> Li Cheng<sup>2</sup>, and Baowen Li<sup>3,†</sup>

<sup>1</sup>*Laboratory of Science and Technology on Integrated Logistics Support, College of Intelligent Science, National University of Defense Technology, Changsha, Hunan 410073, China*

<sup>2</sup>*Department of Mechanical Engineering, Hong Kong Polytechnic University, Hong Kong, China*

<sup>3</sup>*Paul M Rady Department of Mechanical Engineering and Department of Physics, University of Colorado, Boulder, Colorado 80309, USA*

(Received 28 September 2020; revised 5 April 2021; accepted 16 April 2021; published 12 May 2021)

The study of nonreciprocal wave propagation is of great interest for both fundamental research and engineering applications. Here we demonstrate theoretically and experimentally a bidirectional, nonreciprocal, and high-quality diode that can rectify elastic waves in both forward and backward directions in an elastic metamaterial designed to exhibit enhanced nonlinearity of resonances. This diode can preserve or vary frequency, rectify low-frequency long wave with small system size, offer high-quality insulation, can be modulated by amplitude, and break reciprocity of both the total energy and fundamental wave. We report three mechanisms to break reciprocity: the amplitude-dependent band gap combining interface reflection, chaotic response combining linear band gap, amplitude-dependent attenuation rate in damping diode. The bidirectional diode paves ways for mutually controlling information and energy transport between two sources, which can be used as wave insulators.

DOI: 10.1103/PhysRevApplied.15.054022

### I. INTRODUCTION

Diode, a one-way nonreciprocal road for energy transport, plays a pivotal role in electronics [1,2]. Recent years have witnessed the extension of the concept to heat conduction [3–5] and elastic wave manipulation [6–8]. Major concerns of an elastic diode pertaining to practical applications include the frequency range, frequency variation, size-wavelength ( $\lambda$ ) ratio, and insulation quality characterized by the transmission difference  $\Delta T = |T_F - T_B|$ , where  $T_F$  ( $T_B$ ) is the forward (backward) transmission. Several mechanisms have been proposed to realize nonreciprocal elastic wave propagation [8–10].

Topological states offer nonreciprocity in linear elastic systems [11–16] by beating time reversibility with active control or external field, while it is challenging to realize this mechanism in the broad and low frequencies [17–19]. Moreover, this manipulation relies on active control or external field.

Nonlinearity has been demonstrated to offer robust diode effect in two ways: harmonic generation and bifurcation [7,20–23]. In an acoustic diode that consists of a segment of nonlinear medium and a segment of linear phononic crystal, high-order harmonics are generated in the nonlinear medium and the band gap of the phononic crystal

entails asymmetric transfer of the total energy [7,24]. However, this diode [7] causes a frequency change in the output signal as compared with the input one [25], which results in information loss. Moreover, the thickness of this diode [7] is typically approximately  $30\lambda$ , a very large size for low-frequency sound or vibration. The bifurcation-induced elastic diode can realize the frequency-preserved effect, while experimental realizations based on granular chains require a thickness of approximately  $10\lambda$  [20,26,27]. Actively shifting the band gap of a time-variation metamaterial can also induce nonreciprocity [28–31], but the insulation is limited to  $\Delta T \approx 7$  dB with a size of approximately  $5\lambda$  [32]. Moreover, studies should clearly distinguish nonreciprocity of the total energy and fundamental wave.

An open and crucial question is how to design an integrated high-quality, low-frequency, frequency-preserved, and small elastic diode. The critical component to solve this problem is the provision of resonators with enhanced nonlinearity and a mechanism for frequency preservation. Moreover, although bidirectional diodes are readily available in electronics, existing elastic diodes are only unidirectional, namely, they allow energy and information flow only in one direction.

This paper shall demonstrate both theoretically and experimentally a type of elastic diode—frequency-preserved bidirectional diode. The reciprocal transports of total energy and fundamental wave are broken in both

\*wenjihong@vip.sina.com

†baowen.li@colorado.edu

directions. Furthermore, this high-quality diode allows for low-frequency wave rectification with a thickness of approximately  $\lambda$ . The achieved bidirectional diode opens horizons for broad engineering applications as well as the exploration of physics.

## II. MODEL AND METHODS

Our bidirectional diode consists of one segment of linear elastic metamaterial (LEM) [33,34] and one segment of nonlinear elastic metamaterial (NEM) with enhanced nonlinearity, as illustrated in Fig. 1. This NEM offers many fascinating features [35,36], including generating a low-frequency, self-modulated, amplitude-dependent nonlinear locally resonant (NLR) band gap and chaotic responses. The sophisticated triatomic NEM reported in Ref. [37] is adopted to realize the critical mechanisms and it contains ten metacells.

The forward direction is the case where the incident wave arriving from the left terminal first enters the LEM

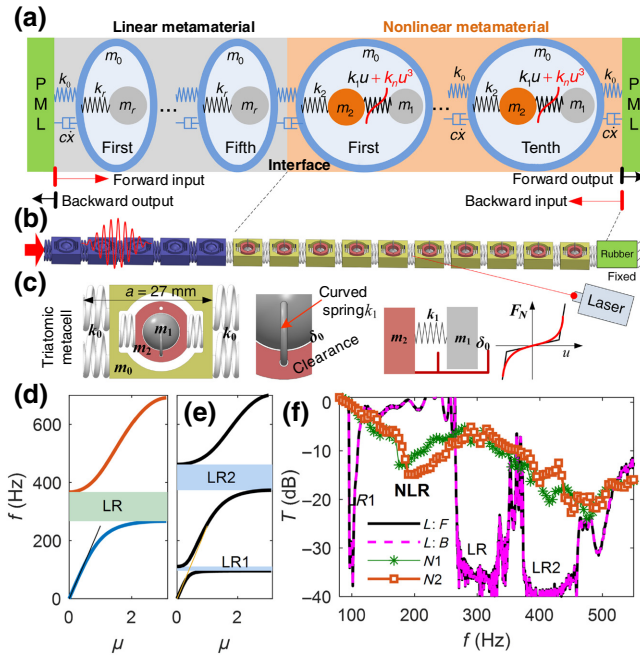


FIG. 1. Elastic diode. (a) Schematic diagram of our bidirectional diode consisting of the LEM (left) and NEM (right). (b) Experimental setup of the diode. Only the forward propagation is indicated and the backward is similar. (c) Structure of the nonlinear triatomic metacell and its equivalent mathematical model. (d), (e) Dispersion curves of the linearized diatomic and triatomic EMs, respectively. (f) Numerical transmissions: here, “L: F” and “L: B” denote the forward and backward transmission of the linearized model, respectively. “N1” and “N2” correspond to transmissions only in the NEM (without LEM) for the incident amplitude  $A_0 = 40$  and  $60 \mu\text{m}$ , respectively, where the amplitude dependence is seen. In (f), the damping coefficient  $c_0 = 3 \times 10^{-5} \text{ s}$ .

[Fig. 1(a)]. Conversely, the backward corresponds to the case when the input wave first enters the NEM. In such a metacell [Fig. 1(c)], the primary oscillator  $m_0$  is a hollowed parallelepiped, and two neighboring  $m_0$  units are coupled through a pair of springs whose entire stiffness is  $k_0$ . The hollow cylinder  $m_2$  held inside  $m_0$  has a hole whose radius is 4.045 mm.  $m_2$  couples to  $m_0$  by two springs with total stiffness  $k_2$ . A steel sphere  $m_1$  is held at the center point of the cylindroid cavity in  $m_2$ , and the two are connected by a curved spring whose stiffness is  $k_1$ . A tiny clearance  $\delta_0 = 45 \pm 15 \mu\text{m}$  between  $m_1$  and  $m_2$  is tactically created to generate enhanced nonlinearity through vibration collision. As detailed in Appendix A, the nonlinear stiffness coefficient reaches  $k_N > 3 \times 10^{12} \text{ N/m}^3$  if we equivalent this clearance nonlinearity to a smooth cubic nonlinearity.

The equations of motion for the individual masses of the  $n$ th triatomic cell are

$$\begin{aligned} m_0 \ddot{u}_n &= k_0(u_{n+1} + u_{n-1} - 2u_n) \\ &+ c_0 k_0(\dot{u}_{n+1} + \dot{u}_{n-1} - 2\dot{u}_n) + k_2(z_n - u_n) \\ m_1 \ddot{y}_n &= -k_1(y_n - z_n) - F_N(t) \\ m_2 \ddot{z}_n &= -k_2(z_n - u_n) + k_1(y_n - z_n) + F_N(t) \end{aligned} . \quad (1)$$

Here,  $u_n$ ,  $y_n$ , and  $z_n$  denote the barycenter displacements of  $m_0$ ,  $m_1$ , and  $m_2$  in the  $n$ th cell, respectively;  $F_N(t)$  denotes the nonlinear contact force depending on  $\delta_0$ . Unless otherwise specified, a weak viscous damping,  $c_0 k_0$ ,  $c_0 = 3 \times 10^{-5} \text{ s}$ , in the primary chain is taken into consideration in theoretical models. To grasp the general physics, we use a smooth cubic nonlinearity in simulations,  $F_N(t) = k_N(y_n - z_n)^3$ , and specify  $k_N = 3 \times 10^{12} \text{ N/m}^3$ .

The LEM consists of five linear diatomic metacells whose primary structures are identical with that of the triatomic cell. We fix the sphere into the cavity of the cylinder to form the local resonator  $m_r$ , i.e., no clearance here. Therefore, the equations of motion for the  $n$ th diatomic metacell are

$$\begin{cases} m_0 \ddot{u}_n = k_0(u_{n+1} + u_{n-1} - 2u_n) \\ + c_0 k_0(\dot{u}_{n+1} + \dot{u}_{n-1} - 2\dot{u}_n) + k_2(r_n - u_n), \\ m_r \ddot{r}_n = -k_r(r_n - u_n), \quad k_r = k_2 \end{cases} \quad (2)$$

where  $r_n$  denotes the barycenter displacement of  $m_r$ . The parameters are as follows: masses  $m_0 = 5.8$ ,  $m_1 = 2.1$ ,  $m_2 = 2$ ,  $m_r = 3.72 \text{ g}$ ;  $k_r = k_2$ ;  $\omega_i = 2\pi f_i = \sqrt{k_i/m_i}$ ,  $i = 0, 1, 2, r$ , and  $f_0 = 322$ ,  $f_1 = 100$ ,  $f_2 = 390.6$ ,  $f_r = 286.4 \text{ Hz}$ .

Moreover, we adopt the equivalent approach based on the bifurcation of nonlinear resonance to analytically explain the dispersion property of the NEM [37] (see Appendix B). The dispersion equation describes the relationship between the wave vector  $\kappa$  and frequency  $f$ .  $\omega = 2\pi f$ .  $\mu = \kappa a = \mu_R + i\mu_I$ ,  $a = 27 \text{ mm}$  denotes

the lattice constant. Due to the amplitude attenuation,  $\mu_I$  self-adaptively changes with propagation distance,  $n$ . The attenuation from  $(n-1)$ th to  $n$ th metacell is  $A(n)/A(n-1) = \exp[-\mu_I(n)]$ .

There are two types of incident signals: (1) a ten-period sinusoidal packet described by the function  $u_0 = A_0 \sin(\omega t)[1 - \cos(\omega t/10)]/2$ ,  $\omega = 2\pi f$ ; (2) the standard sinusoidal wave,  $u_0 = A_0 \sin(\omega t)$ . Numerical integration method is used to solve the wave propagation in models. We confirm that all simulation processes are convergent. Numerical errors are smaller for inputting the wave packet (than inputting the standard sinusoidal wave). Therefore, we use the wave packet as the incident signal in most cases to obtain the distribution of transmission  $T(f, A_0)$ . The standard sinusoidal wave is input when we need to analyze the frequency spectra. In fact, regularities indicated by the two types of signals are the same.

Moreover, to eliminate any asymmetric transmissions due to boundary conditions, we calibrate the numerical diode model whose both ends are connected to a long perfect match layer (PML) consisting of 120 unit cells [38].

We distinguish the diode effects in time and frequency domains. The time-domain wave amplitude is the peak value of  $u_n(t)$ ,  $A_n^{(\text{time})} = \text{peak}[u_n(t)]$ . The frequency-domain amplitude  $A_n^{(\text{freq})}(f)$  is picked from the spectrum of  $u_n(t)$  at the incident frequency. Transmissions in time and frequency domains are

$$T_{\text{time}}(f, A_0) = 20 \log_{10}[A_{\text{out}}^{(\text{time})}(f)/A_0(f)] \quad (\text{dB}), \quad (3)$$

$$T_{\text{freq}}(f, A_0) = 20 \log_{10}[A_{\text{out}}^{(\text{freq})}(f)/A_0(f)] \quad (\text{dB}), \quad (4)$$

where  $A_{\text{out}}(f)$  is the output wave amplitude. The output port is the 15th  $m_0$  from the exciter. As there are multiple harmonics,  $T_{\text{time}}$  represents the transmission of total energy containing all frequency components;  $T_{\text{freq}}$  represents the transmission of fundamental wave.  $\Delta T = T_F - T_B$ .

### III. BIDIRECTIONAL RECTIFICATION WITH PRESERVED FREQUENCY

As shown in Figs. 1(d)–1(f), the diatomic LEM has a local resonant (LR) band gap within 267–366 Hz, and the linearized triatomic EM exhibits two LR band gaps: LR1 96–110 Hz, LR2 374–462 Hz. The NEM produces a NLR band gap that depends on the incident amplitude  $A_0$ . For example, for  $A_0 = 40 \mu\text{m}$ , NLR appears in 210–275 Hz that is in the passbands of the diatomic and triatomic LEM [37]. The slope of the dispersion curve for  $f \rightarrow 0$  indicates that the wave speed of the long wave is  $v_0 = 1000\pi a$ . In Fig. 1(f), the perfectly symmetric transmission of linear structure also validates the numerical model including the PML, and all three band gaps, LR, LR1, and LR2, are activated to produce significant wave attenuation due to the large attenuation  $\mu_I$  [see Fig. 3(a)].

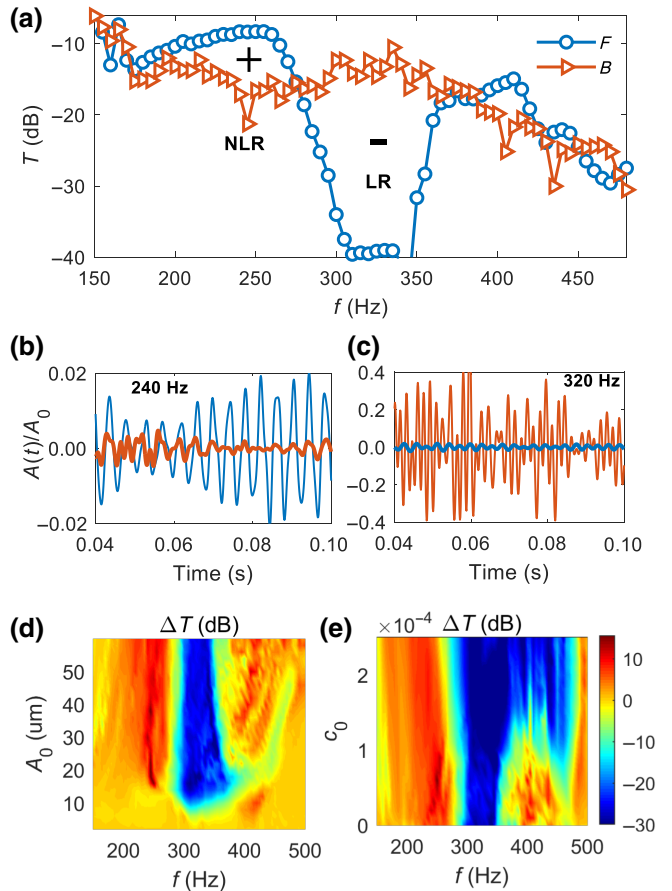


FIG. 2. Numerical results of bidirectional diode. All transmissions denote the time-domain value  $T_{\text{time}}$ . (a) Forward ( $F$ ) transmission  $T_F$  and backward ( $B$ ) transmission  $T_B$ . (b), (c) Time-domain waveforms of the forward and backward transmitted waves for 240 and 320 Hz, respectively. The value  $A(t)/A_0$  is shown here. The colors of curves in (a)–(c) are the same for forward and backward properties. (d), (e) Distributions of  $\Delta T$  versus frequency and  $A_0$  (or  $c_0$ ), respectively. Unless otherwise specified,  $A_0 = 40 \mu\text{m}$  and  $c_0 = 3 \times 10^{-5} \text{ s}$ .

Firstly, we consider  $T_{\text{time}}$ . The transmissions and typical waveforms are shown in Figs. 2(a)–2(c). In the diode, both  $T_F$  and  $T_B$  show attenuations for  $f > 170$  Hz due to enhanced nonlinearity and self-adaptive band-gap effect [37], but the forward and backward reductions are different.  $T_F$  reaches  $-40$  dB in 290–350 Hz due to the LR band gap.  $T_F \approx -10$  dB due to the NLR band gap near 250 Hz. By contrast, the backward waves achieve greater reductions ( $T_B \approx -20$  dB) in the NLR range, but its attenuation in the LR bandgap ( $T_B \approx -15$  dB) is much smaller than  $T_F$ . These observations suggest that our integrated metamaterial breaks reciprocity in both NLR and LR band gaps, and surprisingly, their nonreciprocal directions are opposite, which means that the diode can rectify wave energy in both directions for different frequencies. We call this phenomenon *dual nonreciprocity* or *bidirectional diode*.

As is demonstrated by  $\Delta T(f, A_0)$  in Figs. 2(d) and 2(e), the dual nonreciprocity is enhanced by increasing  $A_0$ , and it can appear without damping. However, increasing the damping can optimize  $\Delta T$  in the NLR range.  $\Delta T$  reaches 1 and  $-30$  dB in NLR and LR ranges, respectively, thus featuring a high-quality diode effect. Moreover, the wavelength in the nonreciprocal band is of  $2.7\pi a < \lambda < 5\pi a$ , which means the thickness of our diode,  $15a$ , is only of approximately  $\lambda$ . Therefore, a small diode is achieved to rectify low-frequency waves by using the subwavelength metacell.

#### IV. PHYSICAL MECHANISMS AND PROPERTIES OF THE DIODE

In order to understand the underlying physics and properties of the diode, we analytically study the amplitude-dependent dispersion relationship  $\mu_I(f)$  of the NEM (Fig. 3). In nonlinear cases, the band near the peak  $\mu_I$  is the NLR band gap shifted from LR1 shown in Fig. 3(a) [37]. The blue shading region 1 in Figs. 3(a) and 3(b) denotes the difference of the attenuation rate  $\Delta\mu_I$  in NLR range, induced by amplitude. The green shading region 2 is  $\Delta\mu_I$  in the passband between the strongly and weakly nonlinear (or linear) metamaterial. In theory, nonreciprocity of fundamental wave is described by  $\Delta\mu_I$  between the forward

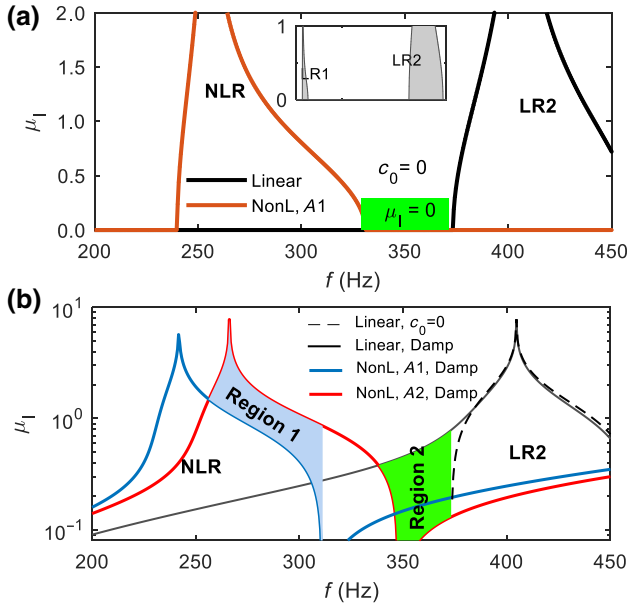


FIG. 3. Mechanisms for nonreciprocity. (a) Analytical dispersion relationship  $\mu_I(f)$  of the undamped metamaterial,  $c_0=0$ . (b)  $\mu_I(f)$  of the damped metamaterial. Here,  $c_0=2 \times 10^{-4}$  s in the damped cases;  $A_1$  ( $A_0=30$   $\mu\text{m}$ ) and  $A_2$  ( $A_0=60$   $\mu\text{m}$ ) represent the moderate and high amplitudes in nonlinear model, respectively.

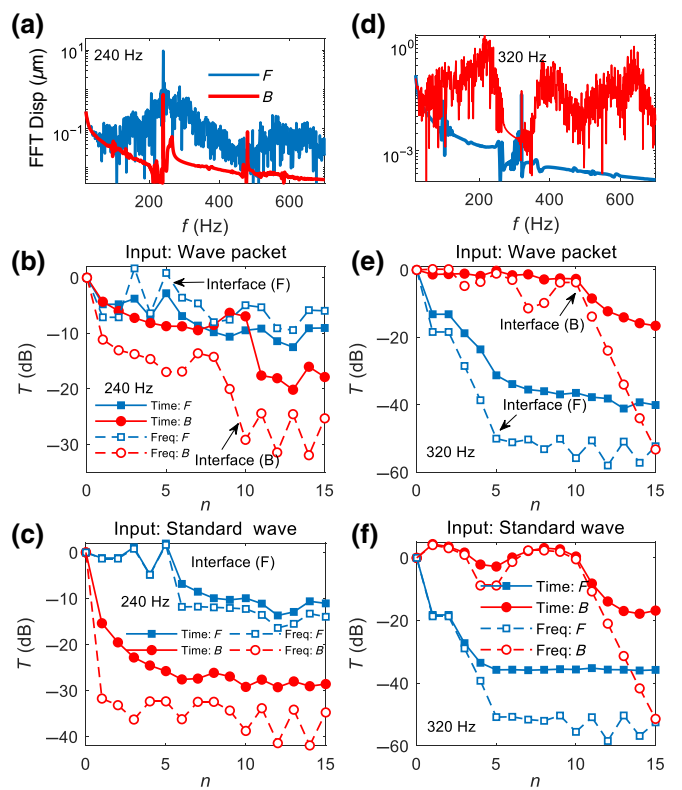


FIG. 4. Properties of the bidirectional diode.  $A_0=40$   $\mu\text{m}$ ,  $c_0=3 \times 10^{-5}$  s if it is constant. (a)–(c) for 240 Hz; (d)–(f) for 320 Hz. (a), (d) Displacement spectra at the 15th cell in forward and backward directions. (b), (e), (c), (f) Transmissions  $\Delta T_{\text{time}}$  and  $\Delta T_{\text{freq}}$  at  $n$ th cell from the incident source. Input waves in (b), (e) are wave packets, and in (c), (f) are monochromatic sinusoidal wave signals.

and backward processes in the NEM:

$$\Delta T_{\text{freq}} = 20 \log_{10} \left\{ \exp \left[ - \sum_{n=1}^{10} \Delta\mu_I(n) \right] \right\} \quad (\text{dB}). \quad (5)$$

In region 2,  $\mu_I = 0$  for  $c_0=0$  [Fig. 3(a)], which means the amplitude has no influence on nonreciprocity in this case.

We perform simulations at typical frequencies to show these nonreciprocal processes. As shown in Fig. 4, the transmissions  $\Delta T_{\text{time}}$  and  $\Delta T_{\text{freq}}$  at  $n$ th cell from the incident source, there are some differences between inputting the aforementioned wave packet and monochromous wave. As analyzed in detail in the Supplemental Material [38], those differences arise from two aspects: (1) the wave packet is a continuous-spectrum signal while the standard sinusoidal wave is monochromous; (2) inputting the monochromous wave may induce standing-wave resonance because of the imperfections of the ‘‘perfectly match layer’’ (i.e., the PML cannot absorb 100% incident energy). Fortunately, properties indicated by the two types of incident signals are the same.

### A. Amplitude-dependent band gap

As illustrated in Fig. 4(a), for waves in the NLR band gap represented by 240 Hz, although the spectrum of the forward transmitted wave is complex and the backward propagation features second-harmonic generation, fundamental wave remains the main component, which highlights a *frequency-preserved single-mode* operation. The varying trends of  $T_{\text{time}}$  and  $T_{\text{freq}}$  in Fig. 4(b) clarify that reciprocity of both the total energy and fundamental wave are broken, and  $\Delta T_{\text{freq}}$  is much higher.

The asymmetric transmission in the NLR band gap originates from the amplitude-dependent property. In the NEM, the initial amplitude in the backward direction is  $A_0$ . At the interface between LEM and NEM, the forward incident wave is partly reflected by NEM due to its NLR band gap [see Figs. 4(b), 4(d), and 3(b)]. Therefore, the initial amplitude of the transmitted wave in NEM is smaller than  $A_0$ . In essence, the amplitude difference between forward and backward directions forms the shading region 1 in Fig. 3(b). According to Eq. (5), nonreciprocity in this range is realized because the attenuation factor  $\Delta\mu_I \neq 0$  between two directions. The backward wave obtains higher attenuation, namely, larger  $\mu_I$  due to higher amplitude.

Furthermore, by describing the offset between  $T_F(A_0)$  and  $T_B(A_0)$ , we present a phenomenological explanation for this nonreciprocal propagation, as shown in Fig. 5. Although the entire nonreciprocity in this range is almost constant [see Fig. 2(a)], the amplitude dependent  $\Delta T_{\text{time}}$  in Fig. 5 fluctuates with  $A_0$ . The positive  $\Delta T_{\text{time}}$  at 40 and 68  $\mu\text{m}$  reaches 20 and 30 dB, respectively: high-quality diode. The transmission of the ten-cell NEM,  $T_{\text{NEM}}$ , decreases with increasing  $A_0$  in whole, but local fluctuations lead to minimal  $T_{\text{NEM}}$ . Because  $T_{\text{NEM}}$  and  $T_B$  follow the same trends including the valleys:  $T_{\text{NEM}} \propto T_B$ . In contrast, at the interface between LEM and NEM, the forward incident wave is partly reflected by NEM due to its NLR band gap. Therefore, the initial amplitude of the

transmitted wave in NEM is smaller than  $A_0$ , so the curve of  $T_F(A_0)$  is shifted to the upper left relative to  $T_B(A_0)$ : the offset between  $T_F(A_0)$  and  $T_B(A_0)$  likes the phase difference between two mathematical functions. Damping in the LAM offers the similar offset effect. As the valley of  $T_B(A_0)$  meets the peak of  $T_F(A_0)$ , significant nonreciprocity is generated. Nevertheless, nonreciprocity diminishes in some amplitude ranges when the peak of  $T_B(A_0)$  meets the valley of  $T_F(A_0)$ .

### B. Chaotic effect

For waves in the LR band, as represented by 320 Hz, the output frequency is changed [see Figs. 2(c) and 4(d)]. Because of the LR band gap, the forward wave is mostly reflected by LEM that leads to a reduction of 40 dB within five cells [see Figs. 4(e) and 4(f) for  $n \leq 5$ ]. Upon entering the triatomic metamaterial, the amplitude of the wave (i.e., the residual energy) is already very small, which can just cause linear or very weak nonlinear effect. Therefore, this wave goes into the passband of the triatomic metamaterial (for  $n > 5$ ) that can go through it with little attenuation. As a result,  $T_F^{\text{time}} \approx -40$  dB, and the frequency remains in this process. However, for backward propagation, the same wave first entering the triatomic metamaterial (for  $n \leq 10$ ) generates enhanced nonlinearity that induces chaotic wave dynamics featuring continuous spectrum [39,40], namely, the entering wave energy spreads over to other frequencies that can go through the LEM [see Fig. 4(d) the red curve]. Changes of  $T_B^{\text{time}}$  with the propagation distance show that the attenuation mainly occurs in the LEM due to the LR band gap. However, the reduction is only 15 dB because the LR cannot effectively reflect the energy with frequencies outside of this band. Consequently, this leads to a rectification of  $|\Delta T_{\text{time}}| > 25$  dB. Therefore, the nonreciprocity in LR is a *single-mode to chaotic continuous-mode* operation.

### C. Damping effect

Here we note that the time-domain value  $T_B^{\text{time}}$  represents the transmission of total wave energy that contains all frequency components. The frequency-domain value  $T_{\text{freq}}$  represents the transmission of a single frequency component, i.e., only observe the energy at the incident frequency  $f$  and do not consider other components in chaotic waves. Different from the time-domain property in LR band gaps, we have  $T_F^{\text{freq}} \approx T_B^{\text{freq}}$  at  $n = 15$  in Figs. 4(e) and 4(f), which indicates that the chaotic mechanism only breaks the reciprocity of total energy while almost preserving reciprocity at fundamental frequency for weak damping. The mechanism for this “abnormal” weak nonreciprocity lies in region 2 in Fig. 3(a). The attenuation property of a frequency component is dominated by the attenuation exponent  $\mu_I$  in the dispersion theory (Appendix B).

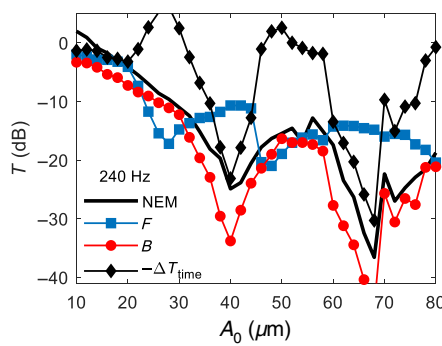


FIG. 5. Transmission  $T_{\text{time}}$  of NEM and  $\Delta T$  of the diode change with  $A_0$  under 240 Hz. To show laws more clearly,  $-T$  is depicted here. Input waves are wave packets.

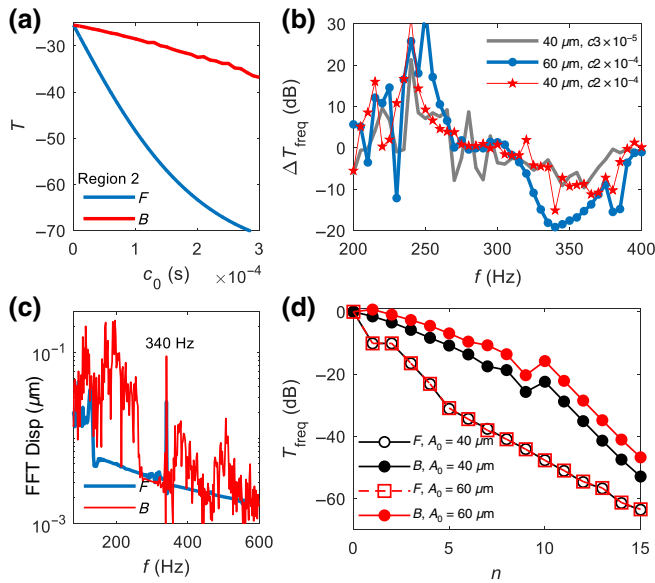


FIG. 6 Wave propagation in the shading region 2. Here we take  $f = 340$  Hz as an example. (a) Analytical transmissions of the diode when changing  $c_0$ ,  $A_0 = 60 \mu\text{m}$ . (b)  $T_{\text{freq}}$  for different damping cases. (c) Frequency spectrum for  $A_0 = 60 \mu\text{m}$ ,  $c_0 = 2 \times 10^{-4}$  s. (d) Propagating processes for  $A_0 = 40$  and  $60 \mu\text{m}$ . Input waves are standard monochromatic signals.

In region 2, if the damping  $c_0 = 0$ ,  $\mu_I$  is zero for both linear and nonlinear metamaterials, so that the difference of attenuation exponent  $\Delta\mu_I$  between the forward and backward propagations remains zero (i.e.,  $\Delta\mu_I = 0$  for  $c_0 = 0$ ). This means that, in the ideal case without considering the harmonic generation in the chaotic process, the single component in the continuous spectrum (320 Hz here) undergoes the same process in forward and backward directions. Thus, according to Eq. (5),  $\Delta T_{\text{freq}} = 0$  and  $T_F^{\text{freq}} \approx T_B^{\text{freq}}$ . In practice, there is weak nonreciprocity that originates from the energy transfer to other bands due to the chaotic effect [see Fig. 6(b) the case  $c_0 = 3 \times 10^{-5}$  s].

Interestingly, according to Eq. (5), by analytically calculating  $\mu_I(n)$  at every metacell, we find that reciprocity of fundamental wave in the LR band can be broken by increasing the damping, as shown in Fig. 6(a). Numerical results in Figs. 6(b)–6(d) confirm this property. The secret still lies in the shading region 2:  $\Delta\mu_I \neq 0$  between the strongly nonlinear case (i.e., the backward propagation) and weakly nonlinear case (i.e., the forward propagation) if there is damping. Moreover, increasing damping can highlight the fundamental wave from the chaotic spectrum [Fig. 6(c)]. The maximum  $\Delta T_{\text{freq}}$  appears near 340 Hz in Fig. 6(b) because the valley value  $\mu_I \rightarrow 0$  is here.

#### D. Subwavelength diode

The bidirectional nonreciprocity stated above are reported with the diode model consisting of five diatomic

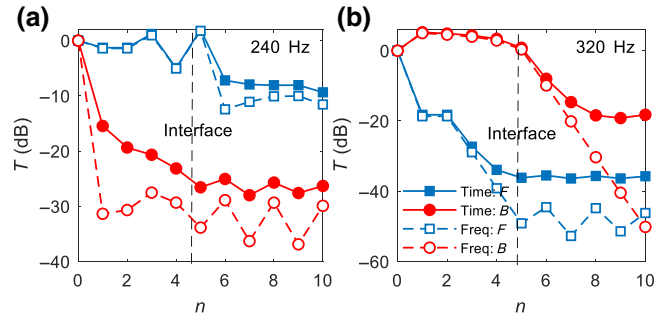


FIG. 7. Nonreciprocal properties for the diode model consisting of five diatomic and five triatomic metacells. Input waves are standard sinusoidal waves.  $A_0 = 40 \mu\text{m}$  and  $c_0 = 3 \times 10^{-5}$  s. (a) 240 Hz. (b) 320 Hz.

and ten triatomic metacells (i.e., a “5 + 10” model). Actually, a shorter diode, e.g., the “5 + 5” model with approximately 0.67 wavelength, can also offer highly efficient nonreciprocal wave control, as shown in Fig. 7. The properties are the same as the laws in Figs. 4(c) and 4(f).

#### E. Wave interference

Moreover, as shown in Figs. 4(f) and 7(b), when inputting the standard sinusoidal wave at 320 Hz, the backward transmission at some positions  $n$  slightly exceeds 1 (i.e., 4 dB). This is the interference between the incident

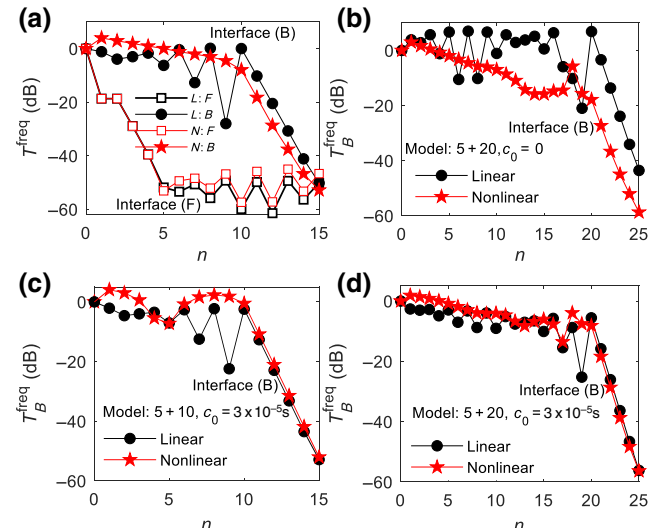


FIG. 8. Wave interference in the diode at 320 Hz,  $A_0 = 40 \mu\text{m}$ . (a), (c) The model consisting of five diatomic and ten triatomic metacells. (b), (d) The model consisting of five diatomic and 20 triatomic metacells. (a), (b) Undamped cases. (b), (c) Cases for weak damping  $c_0 = 3 \times 10^{-5}$  s. Here, all signals are analyzed in frequency domain, and only the backward transmissions  $T_B^{\text{freq}}$  are shown (b)–(d). Linear ( $L$ ) and nonlinear ( $N$ ) model denote the cases  $k_N = 0$  and  $k_N = 3 \times 10^{12} \text{ N/m}^3$  in triatomic metacells, respectively.

wave and the reflected wave from the interface between the triatomic and diatomic segments. The evidences are shown in Fig. 8. Two models with different lengths “5 + 10” and “5 + 20” are analyzed here. In the backward direction [Figs. 8(a) and 8(b)], the wave amplitude in the linear triatomic segment experiences much greater fluctuation (especially near the interface) than that in the nonlinear model because nonlinearity reduces the interference. Whereas in forward direction [Fig. 8(a)], waves in both the linear model (i.e., the model for  $k_N = 0$  in the triatomic segment) and the nonlinear model experience the same fluctuation because the amplitude becomes so small that linearity dominates the dynamics.

Moreover, as shown in Figs. 8(c) and 8(d), damping can weaken the fluctuation in the linear model, but it enhances the fluctuation in the “5 + 10” nonlinear model [see Fig. 8(c)] because damping can weaken the waveform distortion to a certain extent. When increasing the length of the triatomic segment to 20 metacells [Fig. 8(d)], this phenomenon disappears in  $5 < n < 20$  but the  $T_B > 1$  remains in  $0 < n < 5$ . Combining Figs. 7(b), 8(c) and 8(d), the phenomenon for  $T_B > 1$  appears near the source, and becomes remarkable in short diodes. Moreover, this phenomenon has little influence on the diode efficiency concerned in this paper.

## V. EXPERIMENTS

Analyses above are made based on the model including smooth nonlinearity. The diode model containing clearance nonlinearity and weak damping is also numerically analyzed. As shown in Fig. 9, the clearance nonlinearity can repeat the bidirectional diode effect.

### A. Experimental methods

We conduct experiments to demonstrate the performance of the bidirectional diode, as shown in Fig. 10. In the diode, the sphere and springs are made of steel; the hollowed parallelepiped and cylinder are made of aluminum alloy. We suspend the diode in a smooth guide rail through strings to reduce the friction between the diode and the rail.

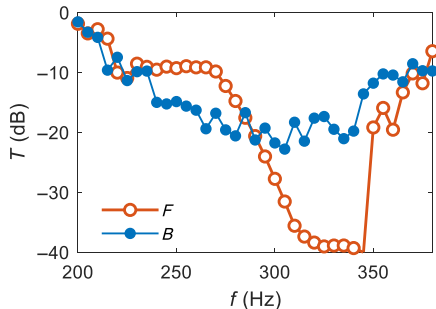


FIG. 9. Numerical results for the model containing clearance nonlinearity.  $A_0(f) = 60 \mu\text{m}$  and  $c_0 = 3 \times 10^{-5} \text{ s}$ .

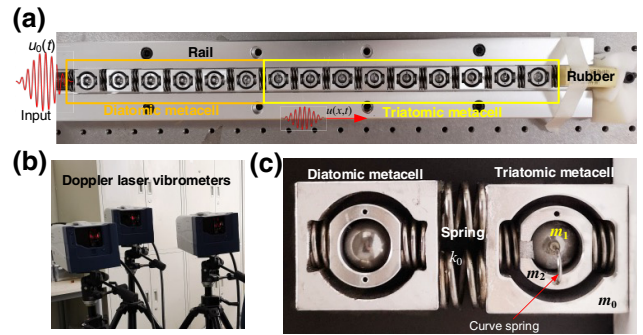


FIG. 10. Experiments. (a) Experiment setup. (b) The Doppler laser vibrometers used in experiment. (c) Pictures of the diatomic and triatomic metacells.

The left end of the diode is connected to an electromagnetic vibration exciter and the other end is fixed. A rubber is connected to the diode to reduce the boundary reflections. Three Doppler laser vibrometers are used to measure the input and two output points, synchronously. The directly measured signal is the velocity,  $v(t)$ , and the displacement is  $u(t) \approx v(t)/2\pi f$  for the frequency  $f$ . The driving levels are tuned by the voltage of the amplifier for the electromagnetic excitor. Under a driving level, the power of the amplifier is constant such that the driving amplitude  $A_0$  decreases as the central frequency  $f$  increases, as shown in Fig. 11.

We still use sinusoidal wave packet as the input signal but the waveform is optimized in experiment. It is still ten periods of packet. Here, the middle eight periods feature the constant amplitude  $A_0$ ; the initial and the cutoff ends are smoothed to eliminate the impact wave induced by the jumping of amplitude. The peak amplitude of the transmitted packet in time domain is  $A$ , and the transmission denotes  $T = A/A_0 = V/V_0$ . As shown in Fig. 11, although there are influences of dispersion and subsequent

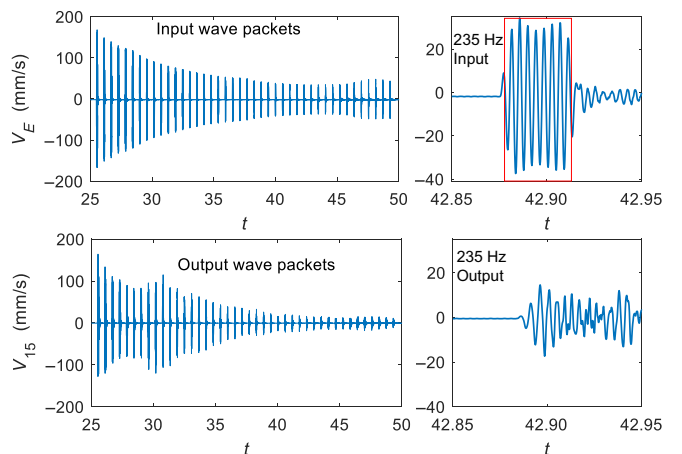


FIG. 11. Typical exciting and output signals,  $V_E$  and  $V_{15}$ , at 5 V. Signals at 235 Hz are enlarged.

vibrations when the incident packet is terminated, the peak value of the output packet can be clearly picked. Enough time interval, 0.5 s, between two packets is taken to make sure that the former packet will not influence the response of the next packet.

## B. Experimental demonstration

Experimental results are shown in Fig. 12. In the case with sinusoidal packet input, experiments under two excitation levels, 5, 9 V, are performed to give rise to the NLR band gap in 200–275 Hz. The experimental trends in Figs. 12(a) and 12(b) agree very well with the numerical results in Figs. 2 and 9.  $\Delta T$  in LR and NLR, respectively, reaches -40 and 20 dB, which demonstrate the high-quality insulation.

Besides the sinusoidal packet, a sweep-amplitude signal at a given frequency (235 or 320 Hz) but with time-varying

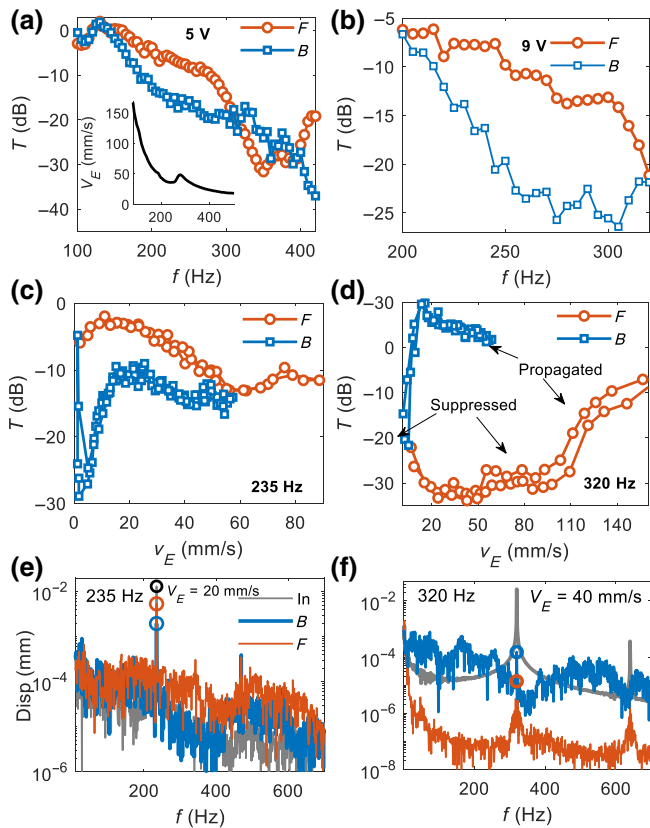


FIG. 12. Experimental demonstrations. Inputs in (a), (b) are wave packets, in (c), (d) are sweep-amplitude signals, and in (e), (f) are sinusoidal signal with constant amplitude. (a) Results for level 5 V. (b)  $T$  for level 9 V. The inset in (a) is the input velocity  $V_E$  for level 5 V. Transmissions varying against  $V_E$  at frequency (c) 235 and (d) 320 Hz. Two curves of each  $T_F$  or  $T_B$  correspond to ascending and descending processes. These transmissions are calculated in time domain. (e), (f) Frequency spectra of the input forward and backward transmitted wave. Circles are the peak value at fundamental frequency.

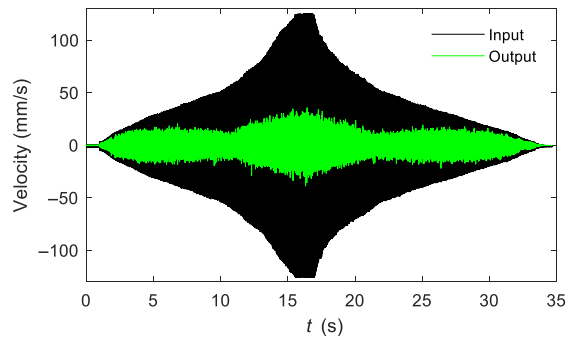


FIG. 13. Signals for sweep-amplitude experiment.

amplitude is also adopted in experiments, as shown in Fig. 13. Here, the transmission is calculated in different time intervals:

$$T(t, t + \Delta t) = 20 \log_{10}[A_{\text{out}}(t, t + \Delta t)/A_0(t, t + \Delta t)] \quad (\text{dB}),$$

where  $X(t, t + \Delta t)$  denotes the maximum value in the time interval  $(t, t + \Delta t)$ . As shown in Figs. 12(c) and 12(d), this experiment clearly describes the variation laws of the asymmetric transmission. We still show  $T_{\text{time}}$  first.  $\Delta T$  of the bidirectional diode is tunable by driving amplitude. When the incident velocity  $V_E \rightarrow 0$ , transmissions in both NLR and LR bands are symmetric due to linearity. Owing to the tiny clearance, small amplitude drives the metamaterial to generate enhanced nonlinearity, on which occasion reciprocities in both NLR and LR are broken. Positive  $\Delta T$  at 235 Hz reaches 20 dB for a small amplitude  $V_E \approx 5$  mm/s; after that,  $T_B$  firstly increases and then decreases as  $V_E$  ascends, but  $T_F$  mainly behaves a descending trend because of the frequency shift of the peak  $\Delta T$ . However, the nonreciprocity at 235 Hz almost disappears near  $V_E \approx 60$  mm/s ( $A_0 \approx 40$   $\mu\text{m}$ ), which demonstrates the amplitude-dependent trends shown in Fig. 5.

In the LR band gap represented by 320 Hz, the forward propagation remains suppressed when  $V_E < 110$  mm/s ( $A_0 < 55$   $\mu\text{m}$ ), but  $T_B$  jumps to a large value (-10 dB) at a small amplitude  $V_E = 13$  mm/s ( $A_0 \approx 6.5$   $\mu\text{m}$ ): a significant negative rectification  $\Delta T \approx -40$  dB is achieved. Moreover, for  $A_0 > 55$   $\mu\text{m}$ ,  $T_F$  jumps to a large value and increases with  $V_E$  on which occasion the forward energy starts to transfer.

Under typical amplitudes that can generate nonreciprocity, we analyze the spectra with constant sinusoidal inputs, as shown in Figs. 12(e) and 12(f). Figure 12(e) demonstrates that nonreciprocity in the NLR band preserves the frequency, and reciprocity of fundamental wave is also broken (see the peaks). In Fig. 12(f), the continuous spectrum of the backward wave confirms the chaotic property; although the fundamental wave is not the main component, reciprocity of fundamental wave is also broken. These results are consistent with theories.

## VI. CONCLUSIONS

In conclusion, we demonstrate theoretically and experimentally the frequency-preserved, bidirectional, high-quality, low-frequency, small size (approximately one wavelength and can be subwavelength), and tunable elastic diode. This is achieved by using elastic metamaterial with the intentional clearance inside metacells to create enhanced nonlinearity. Their transmission differences reach as much as 20 dB and -40 dB, respectively. We report three nonreciprocal mechanisms. The amplitude-dependent band gap combining the interface reflection enables the frequency-preserved nonreciprocity of both the total energy and fundamental wave. The linear band gap combining with the chaotic responses performs the monochromatic-to-continuous nonreciprocity of total energy, while the propagation for fundamental wave is weakly nonreciprocal under weak damping. Increasing damping can break both types of reciprocity in the same band. Our study finds physics, and paves ways to conceive devices and metamaterials for asymmetric energy transmissions with reversible rectifying direction.

## ACKNOWLEDGMENTS

X.F. and J.-H.W. are funded by the National Natural Science Foundation of China (Projects No. 12002371, No. 11991032, and No. 11991034).

## APPENDIX A: NONLINEARITY

In experiments, the nonlinear force  $F_N(t)$  generated by the contact between the sphere and the hollow cylinder is a piecewise nonlinear function

$$F_N(t) = \begin{cases} k_1 u & \text{for } |u| \leq \delta_0 \\ k_1 u + A_c(u - \delta_0)^{3/2} & \text{for } u > \delta_0 \\ -k_1 u - A_c(-u - \delta_0)^{3/2} & \text{for } u < -\delta_0 \end{cases}. \quad (\text{A1})$$

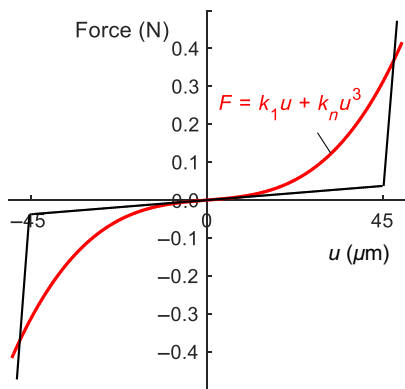


FIG. 14 The nonlinear forces-deformation curves. The black curve is the piecewise function.

Here,  $\delta_0$  denotes the width of the clearance and  $A_c = 2E_s\sqrt{r_s}/[3(1 - \nu^2)]$ , where  $E_s$  and  $\nu$  represent the elastic modulus and Poisson's ratio of the softer medium, respectively.  $E_s = 70$  GPa,  $\nu = 0.3$ . The piecewise function  $F_N(t)$  described by Eq. (A1) can be fitted with a smooth equation  $k_1 u + k_N u^{3/2}$ . The linear coefficient,  $k_1$ , is constant but the nonlinear coefficient,  $k_N$ , depends on the clearance,  $\delta_0$ . As shown in Fig. 14, by fitting the curve, one can use the cubic nonlinear equation to approximate the piecewise function, and  $k_N \approx 3 \times 10^{12}$  N/m<sup>3</sup>.

## APPENDIX B: DISPERSION THEORY

The dispersion relationship of the linear diatomic metamaterial is

$$\cos \mu = 1 - \frac{\omega^2 m_0}{2k} - \frac{\omega^2 \omega_r^2 m_r}{2k(\omega_r^2 - \omega^2)}, \quad (\text{B1})$$

where  $k = k_0(1 + i\omega c_0)$ ;  $\mu = \kappa a$ ;  $\kappa$  is the wave vector and  $a = 27$  mm is the lattice constant. The dispersion curve of the linear diatomic metamaterial is shown in Fig. 15. The dispersion relationship of the linear triatomic metamaterial is

$$\cos \mu = 1 - \frac{m_0 \omega^2}{2k} - \frac{\omega^2 \omega_2^2 [m_1 \omega_1^2 + m_2 (\omega_1^2 - \omega^2)]}{2k[m_2(\omega^2 - \omega_1^2)(\omega^2 - \omega_2^2) - m_1 \omega^2 \omega_1^2]}. \quad (\text{B2})$$

For the nonlinear triatomic metamaterial, we adopt the equivalent linearized approach based on the bifurcation of nonlinear local resonance to solve the dispersion effect. This approach is proposed in Ref. [37]. Similar with

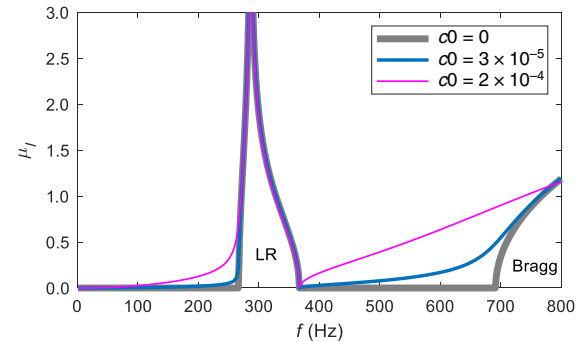


FIG. 15 Dispersion curve of the linear diatomic metamaterial.

Eq. (B2), we have

$$\cos \mu = 1 - \frac{m_0 \omega^2}{2k} - \frac{\omega^2 \omega_2^2 [m_1 \omega_{1e}^2 + m_2 (\omega_{1e}^2 - \omega^2)]}{2k [\omega^2 - \omega_{1e}^2] (\omega^2 - \omega_2^2) - m_1 \omega^2 \omega_{1e}^2}. \quad (B3)$$

Here,  $\omega_{1e}$  is the equivalent nature frequency of oscillator  $m_1$ . It is solved with the bifurcation analysis. The nonlinear local resonance in the triatomic metacell can be solved with the first-order harmonic balance method. The equation is

$$\begin{cases} \omega^2 m_1 Y = k_1 P + 3k_N P^3 / 4 \\ (k_2 - \omega^2 m_2)(Y - P) - \omega^2 m_1 Y = k_2 A_0. \end{cases} \quad (B4)$$

This equation is obtained by specifying  $u = A_0 \sin \omega t$ ,  $y = Y \sin \omega t$ ,  $z = Z \sin \omega t$ ,  $P = Y - Z$ , in Eq. (1). For specified incident amplitude  $A_0$ , one obtains the saddle-node bifurcation point of the first nonlinear resonance. The solution of this point is  $(\omega_{J1}, P_{J1})$  [See Fig. 1(c) in Ref. [37]]. The equivalent stiffness and nature frequency of the nonlinear oscillator  $m_1$  is

$$k_{1e} = k_1 + 3k_N P_{J1}^2 / 4, \quad \omega_{1e} = \sqrt{k_{1e}/m_1}. \quad (B5)$$

By specifying the frequency  $\omega$ , one can solve  $\mu = \mu_R + i\mu_I$ . The imaginary part  $\mu_I$  characterize the wave attenuation. Moreover, based on Eqs. (B1) and (B3), we can calculate  $\mu_I$  at every unit cell in the elastic diode. Then, we can obtain the forward and backward transmissions by using the attenuation  $\exp[-\mu_I(n)]$ . The reflection at the interface is not considered.

- [1] M. O. Kolawole, *Electronics: From Classical to Quantum* (CRC Press, Boca Raton, 2020).
- [2] M. C. Gupta and J. Ballato, *The Handbook of Photonics* (CRC Press, Boca Raton, 2021), 2nd ed.
- [3] B. Li, L. Wang, and G. Casati, Thermal Diode: Rectification of Heat Flux, *Phys. Rev. Lett.* **93**, 184301 (2004).
- [4] N. Li, J. Ren, L. Wang, G. Zhang, P. Hänggi, and B. Li, Colloquium: Phononics: Manipulating heat flow with electronic analogs and beyond, *Rev. Mod. Phys.* **84**, 1045 (2012).
- [5] G. Wehmeyer, T. Yabuki, C. Monachon, J. Wu, and C. Dames, Thermal diodes, regulators, and switches: Physical mechanisms and potential applications, *Appl. Phys. Rev.* **4**, 041304 (2017).
- [6] V. F. Nesterenko, C. Daraio, E. B. Herbold, and S. Jin, Anomalous Wave Reflection at the Interface of Two Strongly Nonlinear Granular Media, *Phys. Rev. Lett.* **95**, 158702 (2005).

- [7] B. Liang, X. S. Guo, J. Tu, D. Zhang, and J. C. Cheng, An acoustic rectifier, *Nat. Mater.* **9**, 989 (2010).
- [8] H. Nassar, B. Yousefzadeh, R. Fleury, M. Ruzzene, A. Alù, C. Daraio, A. N. Norris, G. Huang, and M. R. Haberman, Nonreciprocity in acoustic and elastic materials, *Nat. Rev. Mater.* **5**, 667 (2020).
- [9] G. Wu, Y. Long, and J. Ren, Asymmetric nonlinear system is not sufficient for a nonreciprocal wave diode, *Phys. Rev. B* **97**, 205423 (2018).
- [10] A. A. Maznev, A. G. Every, and O. B. Wright, Reciprocity in reflection and transmission: What is a ‘phonon diode’?, *Wave Motion* **50**, 776 (2013).
- [11] A. Souslov, B. C. van Zuiden, D. Bartolo, and V. Vitelli, Topological sound in active-liquid metamaterials, *Nat. Phys.* **13**, 1091 (2017).
- [12] H. He, C. Qiu, L. Ye, X. Cai, X. Fan, M. Ke, F. Zhang, and Z. Liu, Topological negative refraction of surface acoustic waves in a Weyl phononic crystal, *Nature* **560**, 61 (2018).
- [13] A. Y. Song, X. Q. Sun, A. Dutt, M. Minkov, C. Wojcik, H. Wang, I. Williamson, M. Orenstein, and S. Fan, PT-Symmetric Topological Edge-Gain Effect, *Phys. Rev. Lett.* **125**, 033603 (2020).
- [14] H. Xue, Y. Yang, G. Liu, F. Gao, Y. Chong, and B. Zhang, Realization of an Acoustic Third-Order Topological Insulator, *Phys. Rev. Lett.* **122**, 244301 (2019).
- [15] E. Riva, M. I. N. Rosa, and M. Ruzzene, Edge states and topological pumping in stiffness-modulated elastic plates, *Phys. Rev. B* **101**, 094307 (2020).
- [16] S. Li, I. Kim, S. Iwamoto, J. Zang, and J. Yang, Valley anisotropy in elastic metamaterials, *Phys. Rev. B* **100**, 195102 (2019).
- [17] M. Miniaci, R. K. Pal, B. Morvan, and M. Ruzzene, Experimental Observation of Topologically Protected Helical Edge Modes in Patterned Elastic Plates, *Phys. Rev. X* **8**, 031074 (2018).
- [18] M. I. N. Rosa, R. K. Pal, J. R. F. Arruda, and M. Ruzzene, Edge States and Topological Pumping in Spatially Modulated Elastic Lattices, *Phys. Rev. Lett.* **123**, 034301 (2019).
- [19] Q. Wu, H. Chen, X. Li, and G. Huang, In-Plane Second-Order Topologically Protected States in Elastic Kagome Lattices, *Phys. Rev. Appl.* **14**, 014084 (2020).
- [20] N. Boechler, G. Theocharis, and C. Daraio, Bifurcation-based acoustic switching and rectification, *Nat. Mater.* **10**, 665 (2011).
- [21] J. Bunyan, K. J. Moore, A. Mojahed, M. D. Fronk, M. Leamy, S. Tawfick, and A. F. Vakakis, Acoustic nonreciprocity in a lattice incorporating nonlinearity, asymmetry, and internal scale hierarchy: Experimental study, *Phys. Rev. E* **97**, 052211 (2018).
- [22] I. Grinberg, A. F. Vakakis, and O. V. Gendelman, Acoustic diode: Wave non-reciprocity in nonlinearly coupled waveguides, *Wave Motion* **83**, 49 (2018).
- [23] A. S. Gliozi, M. Miniaci, A. O. Krushynska, B. Morvan, M. Scalerandi, N. M. Pugno, and F. Bosia, Proof of concept of a frequency-preserving and time-invariant metamaterial-based nonlinear acoustic diode, *Sci. Rep.* **9**, 9560 (2019).
- [24] C. Fu, B. Wang, T. Zhao, and C. Q. Chen, High efficiency and broadband acoustic diodes, *Appl. Phys. Lett.* **112**, 051902 (2018).

- [25] Z. Li, B. Yuan, Y. Wang, G. Shui, C. Zhang, and Y. Wang, Diode behavior and nonreciprocal transmission in nonlinear elastic wave metamaterial, *Mech. Mater.* **133**, 85 (2019).
- [26] C. Liu, Z. Du, Z. Sun, H. Gao, and X. Guo, Frequency-Preserved Acoustic Diode Model with High Forward-Power-Transmission Rate, *Phys. Rev. Appl.* **3**, 064014 (2015).
- [27] J. Cui, T. Yang, and L. Chen, Frequency-preserved nonreciprocal acoustic propagation in a granular chain, *Appl. Phys. Lett.* **112**, 181904 (2018).
- [28] H. Nassar, H. Chen, A. N. Norris, M. R. Haberman, and G. L. Huang, Non-reciprocal wave propagation in modulated elastic metamaterials. Proceedings of the Royal Society A: Mathematical, Phys. Eng. Sci. **473**, 20170188 (2017).
- [29] G. Trainiti and M. Ruzzene, Non-reciprocal elastic wave propagation in spatiotemporal periodic structures, *New J. Phys.* **18**, 083047 (2016).
- [30] J. Huang and X. Zhou, A time-varying mass metamaterial for non-reciprocal wave propagation, *Int. J. Solids Struct.* **164**, 25 (2019).
- [31] P. A. Deymier, V. Gole, P. Lucas, J. O. Vasseur, and K. Runge, Tailoring phonon band structures with broken symmetry by shaping spatiotemporal modulations of stiffness in a one-dimensional elastic waveguide, *Phys. Rev. B* **96**, 064304 (2017).
- [32] Y. Chen, X. Li, H. Nassar, A. N. Norris, C. Daraio, and G. Huang, Nonreciprocal Wave Propagation in a Continuum-based Metamaterial with Space-Time Modulated Resonators, *Phys. Rev. Appl.* **11**, 064052 (2019).
- [33] Z. Liu, X. Zhang, Y. Mao, Y. Y. Zhu, Z. Yang, C. T. Chan, and P. Sheng, Locally resonant sonic materials, *Science* **289**, 1734 (2000).
- [34] Y. Wang, H. Zhao, H. Yang, J. Zhong, D. Zhao, Z. Lu, and J. Wen, A tunable sound-absorbing metamaterial based on coiled-up space, *J. Appl. Phys.* **123**, 185109 (2018).
- [35] X. Fang, J. Wen, B. Bonello, J. Yin, and D. Yu, Ultralow and ultra-broad-band nonlinear acoustic metamaterials, *Nat. Commun.* **8**, 1288 (2017).
- [36] O. R. Bilal, A. Foehr, and C. Daraio, Bistable metamaterial for switching and cascading elastic vibrations, *Proc. Natl. Acad. Sci. U. S. A.* **114**, 4603 (2017).
- [37] X. Fang, J. Wen, H. Benisty, and D. Yu, Ultrabroad acoustical limiting in nonlinear metamaterials due to adaptive-broadening band-gap effect, *Phys. Rev. B* **101**, 104304 (2020).
- [38] See Supplemental Material at <http://link.aps.org/supplemental/10.1103/PhysRevApplied.15.054022> for the design of the perfect match layer, and signal processing methods.
- [39] X. Fang, J. Wen, J. Yin, D. Yu, and Y. Xiao, Broadband and tunable one-dimensional strongly nonlinear acoustic metamaterials: Theoretical study, *Phys. Rev. E* **94**, 052206 (2016).
- [40] X. Fang, J. Wen, B. Bonello, J. Yin, and D. Yu, Wave propagation in one-dimensional nonlinear acoustic metamaterials, *New J. Phys.* **19**, 053007 (2017).